# AEROACOUSTIC ANALYSIS OF A TRANSITIONING VECTORED-THRUST/TILT-ROTOR UAM VEHICLE USING THE LB/VLES METHOD

Federico Di Verniere, Emanuele Sticchi, Damiano Casalino, Daniele Ragni, Riccardo Zamponi*

Flow Physics and Technology Department, Delft University of Technology, Kluyverweg 1, Delft, 2629HS, the Netherlands.

*also at Department of Environmental and Applied Fluid Dynamics, von Karman Institute for Fluid Dynamics, Waterloosesteenweg 72, B-1640 Sint-Genesius-Rode, Belgium

## ABSTRACT

A high-fidelity aeroacoustic simulation of a full-scale electric vertical take-off and landing vehicle was performed to investigate the transition maneuver from vertical ascent to forward flight. The study employed a Lattice Boltzmann method, enabling the resolution of complex unsteady aerodynamic phenomena while maintaining manageable computational costs. The analysis revealed that aerodynamic interactions between rotors, nacelles, and the wing significantly affect the distribution of aerodynamic forces, with rotor–wing interference playing a key role in lift and drag behavior. Acoustic emissions were evaluated in the far field using a permeable formulation of the Ffowcs Williams–Hawkings analogy on a spherical array representative of an urban air mobility operational context. The results highlighted clear directional patterns and a harmonic-dominated frequency spectrum. The findings offer critical insights into the coupled aerodynamic and acoustic behavior of eVTOLs during transition and provide a high-fidelity reference to support the validation of lower-order design tools.

## NOTATION

*

Symbols

$b$ Wing Span, m

$C_p$ Pressure Coefficient, $-$

$C_T$ Thrust Coefficient, $-$

$D$ Rotor Diameter, m

$n$ Rotor RPM, Hz

$OASPL$ Overall Sound Pressure Level, dB

$P$ Static Pressure, Pa

$P_\infty$ Free-stream Pressure, Pa

$PWL$ Sound Power Level, dB

$SPL$ Sound Pressure Level, dB

$V_\infty$ Free-stream Velocity Magnitude, m/s

$\gamma_D$ Non-dimensionalized drag, $-$

$\gamma_L$ Non-dimensionalized lift, $-$

$\rho_\infty$ Free-stream Density, kg/m$^3$

$\theta$ Azimuthal position, $^\circ$

*

Acronyms

**BPF** Blade Passing Frequency

**CAA** Computational Aeroacoustics

**CFD** Computational Fluid Dynamics

**FWH** Ffowcs Williams–Hawkings

**eVTOL** electrical Vertical Take-Off and Landing

**MAAS** Multicopter Aero and Acoustic Simulation

**LBM** Lattice Boltzmann Method

**SVS** Smallest Voxel Size

**UAM** Urban Air Mobility

**VLES** Very Large Eddy Simulation

**VR** Voxel Resolution

## INTRODUCTION

Urban air mobility aircraft have gained the spotlight of academic and industrial research in recent years. In fact, new advances in electric propulsion and battery technologies have accelerated their development. Electric propulsion, in particular, aligns very well with the goal of climate-neutral aviation and, at the same time, revolutionizes aircraft design. The Vertical Flight Society's eVTOL Aircraft Directory (Ref. 1) shows how in just ten years the number of prototypes has grown from a few dozen to more than a thousand. The aircraft configurations, cataloged there, are very diverse and differ greatly from traditional rotary-wing aircraft. Among these, one of the most promising designs is the vectored thrust/tilt-rotor type, which employs any of the aircraft's thrusters for lift and cruise. Most implement multiple rotors, a number of which rotate from the vertical direction, for vertical take-off and landing, to the horizontal direction, for cruising. In addition, one or more wings are adopted to improve vehicle performance in the cruise phase.

The transition maneuver from vertical take-off to cruise is a novelty in the rotorcraft scene and represents the peculiarity of this class of vehicles. At the same time, it is also the main challenge in eVTOLs, as it requires a smooth and efficient change in how the aircraft generates lift. To the best of the authors' knowledge, no comprehensive study on the transition maneuver of UAM vectored-thrust / tilt-rotor vehicles is currently available in the literature. An acoustic investigation was carried out by Pascioni et al. (Ref. 2) through a flight test of the Joby Aviation Advanced Air Mobility Prototype Vehicle, from which they suggested that performing the transition from vertical take-off to wing-borne flight in a quick manner could reduce noise emission. Other studies focused only on subcomponents rather than full-scale vehicles, such as the experimental investigation on the aerodynamic interaction of tilted tandem propellers carried out by Zanotti et al. (Ref. 3). On the numerical side, full-scale multi-rotor eVTOLs are mostly investigated in hover conditions, such as the works by Zhang et al. (Ref. 4) and Bao et al. (Ref. 5), who utilize solvers based on Unsteady Reynolds-averaged Navier-Stokes equations.

From an aerodynamic perspective, the unsteady nature of the transition maneuver is directly associated with complex flow phenomena due to the interaction between all elements, such as rotors, wing, and airframe. Accurate modeling and understanding of these effects are essential to ensure efficiency and in-flight stability. In parallel, the acoustic behavior of eVTOL aircraft must be carefully investigated, as the two aspects are intrinsically interconnected. During the transition phase, the redistribution of aerodynamic loads and unsteady flow interactions have a direct influence on the noise generation mechanisms. Understanding the aeroacoustic characteristics of such aircraft is therefore essential to assess their noise emissions in realistic operational conditions.

Given that these vehicles are intended to operate in densely populated urban environments, ensuring low noise emissions is not only desirable but necessary to protect public health. Prolonged exposure to elevated noise levels has been widely recognized as a risk factor for various health issues, including cardiovascular problems (Ref. 6), sleep disturbances, and increased stress levels (Ref. 7). For this reason, regulatory agencies such as the European Union Aviation Safety Agency (Ref. 8) have identified noise as one of the primary challenges to the societal acceptance of UAM vehicles. In this context, characterizing the acoustic footprint of the transition maneuver is particularly relevant. This phase often occurs shortly after take-off, potentially in the heart of urban areas. Understanding the noise implications of this maneuver is therefore key to determining whether it can be safely and acceptably performed within city boundaries, or whether operational constraints must be imposed to minimize acoustic impact.

Furthermore, the noise sources of vectored-thrust eVTOL aircraft differ significantly from those of conventional rotorcraft, as described by NASA's investigations (Ref. 9). In fact, the complex configurations, peculiar to UAM vehicles, lead to unique noise generation mechanisms. Identifying and ranking the dominant noise sources in such configurations would represent a significant advancement for this class of vehicles: it would provide engineers with critical insight to optimize design choices for noise mitigation from the earliest stages of development.

This work performs a detailed aeroacoustic analysis of a full-scale eVTOL aircraft during the transition from vertical to forward flight. By simulating the complete vehicle at scale, the study enables a comprehensive characterization of the dominant aerodynamic phenomena involved in the transition and provides a physically consistent estimation of the noise radiated to the far field. The analysis is conducted on the open-source configuration developed by Wang et al. (Refs. 10, 11) and proposed as a reference for the Delft International Conference on Urban Air Mobility (DICUAM 2026). High-fidelity CFD simulations based on a Very Large Eddy Simulation (VLES) / Lattice-Boltzmann method (LBM) framework are employed, offering a suitable trade-off between computational cost and resolution accuracy, particularly for capturing the flow dynamics relevant to noise generation and propagation. Far-field acoustic prediction is carried out using the permeable Ffowcs Williams-Hawkings (FWH) formulation in the frequency domain (Ref. 12), allowing the evaluation of sound pressure levels and directivity patterns. This analysis provides insights into the aeroacoustic behavior of vectored-thrust eVTOLs during the transition phase, representing a step toward a deeper understanding of the noise generation mechanisms.

## METHODOLOGY

### Flow Solver and Far-Field Acoustics Computation

The high-fidelity Computational Fluid Dynamics (CFD) simulations presented in this study were carried out using the commercial flow solver SIMULIA PowerFLOW®, version 6-2025-R1, developed by Dassault Systèmes. This solver is based on an LBM coupled with a vLES turbulence modeling approach, which allows accurate resolution of unsteady flow features that are critical in aeroacoustic analyses. PowerFLOW has been extensively validated in the literature and has been successfully applied to a wide range of aeroacoustic problems. The solver demonstrated good capabilities to handle flow-induced noise predictions across different levels of complexity, from isolated components to full-scale vehicle configurations (Refs. 13–19). Its ability to capture transient flow phenomena and provide high-resolution surface and volumetric data makes it a suitable tool for aeroacoustic source identification and far-field noise propagation studies in the context of UAM applications (Refs. 20–22).

The flow solver used in this study is inherently well-suited for aeroacoustic simulations due to its low numerical dispersion and dissipation properties (Ref. 23). However, resolving the acoustic field all the way to far-field microphone locations would require prohibitively fine grids, making a direct computation of far-field noise impractical. To overcome this limitation, a hybrid CFD/CAA approach was employed. Specifically, far-field noise was computed using a module from the OptydB toolkit, which provides, among other tools, the permeable surface formulation of the Ffowcs Williams-Hawkings (FW-H) acoustic analogy in the frequency domain (Ref. 12). This formulation generalizes the original approach proposed by Lockard (Ref. 24) to fully three-dimensional flows. It is also consistent with its time-domain counterpart, with the difference that Fourier transforms are applied to the FW-H source terms before their propagation (Ref. 25). The source term spectra were calculated using the Welch method (Ref. 26), applying a Hanning window to temporal segments with a bandwidth of approximately 7 Hz and an overlap coefficient of 0.5.

### Aircraft Geometry and Flight Conditions

The aircraft configuration analyzed in this study is a vectored-thrust eVTOL concept featuring a total of six propellers. These are symmetrically distributed with respect to the longitudinal axis: four are mounted along the main wing (two inboard and two outboard) and two are located on the v-tail. All six propellers are identical and consist of five blades each, with a blade length of 1.58 m.

Each propeller is capable of tilting from a vertical orientation, used during vertical take-off (VTO), to a horizontal orientation for cruise flight. The tilting mechanism, however, differs between rotor positions. On the two tail-mounted propellers and the two outboard propellers on the main wing, both the rotor and its nacelle rotate together as a unit. In contrast, for the two inboard propellers, only the rotor tilts, while the nacelle remains fixed in the horizontal position.

The flight condition investigated corresponds to the transition phase from vertical take-off to cruise, a critical regime for both aerodynamic and aeroacoustic performance. Following a brief preliminary assessment aimed at identifying a condition of balanced aerodynamic forces and moments during the transition maneuver, a free-stream velocity of 40 kts ($20.6\,\mathrm{m\,s^{-1}}$) was selected for the simulation.

To achieve a trimmed flight condition at this velocity, the tilt angles of the rotors were adjusted accordingly. Specifically, the four front propellers were tilted 45° from the vertical, while the two rear propellers were tilted 15° from the vertical. Rotors RPMs are the same for all propellers and have been set to 800. This configuration ensures a representative operating state within the transition regime and allows for detailed analysis of both aerodynamic and acoustic behavior under realistic conditions.

### Simulation Setup

The approach adopted to investigate the transition phase involves modeling the maneuver as a sequence of quasi-steady-state flight/operational conditions, i.e. flight speed and angle of attack, rotors' RPM and tilt angle. This assumption is appropriate for analyzing a slow transition, which inherently minimizes force imbalances associated with fast dynamic effects. Specifically, the condition described in the preceding section is treated as an isolated, fixed-point scenario for the purposes of this analysis. It is also important to highlight that the characteristic timescale of the propeller rotation (0.075 s per revolution) is significantly shorter than that of the overall transition maneuver, which occurs over several seconds. Consequently, in the present study, a duration equivalent to 12 propeller revolutions, corresponding to 0.9 s of real time, was simulated.

The computational domain was established using the Multicopter Aero and Acoustic Simulations (MAAS) workflow for PowerFLOW. The domain encompasses the volume bounded by the aircraft geometry and an outer spherical surface (denoted as VR0), centered at the aircraft's mass center, with a radius equal to 200 times the wing span length. Here, a far-field boundary condition was applied. A sketch of the computational domain is represented in Figure 1a.

No-slip boundary conditions incorporating a turbulent wall model were imposed on all solid surfaces, with the exception of the propeller blades. Here, boundary layer trips were applied at 20% of the chord length to enforce a laminar-to-turbulent transition. Furthermore, an acoustic sponge region was implemented in order to attenuate both outward-propagating and inward-reflected acoustic waves. The sponge region is encompassed by two spherical surfaces, which have a radius of $20\,b$ and $76\,b$, respectively.

The computational domain was discretized into 16 nested resolution regions (VRs), each defined by a uniform grid spacing. The grid resolution coarsened progressively, with the cell size increasing by a factor of two between successive VR levels, from VR15 (finest) to VR0 (coarsest). The resolution levels VR15 through VR11 were defined relative to offsets from the aircraft surface to provide increased spatial resolution in critical flow regions, specifically within the propeller wake and in proximity to aerodynamic surfaces such as the propeller blades and wings. VR10 was defined with a larger offset in order to include the FW-H permeable surface. Finally, VR9 to VR0 consist of concentrical spheres centered in the aircraft's

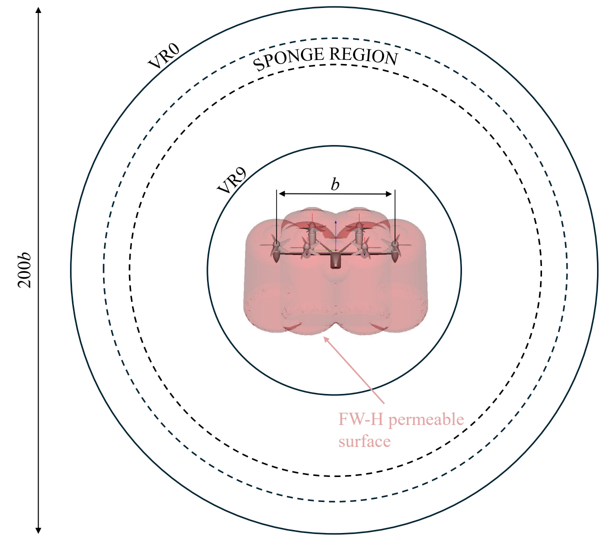


(a) Sketch of the computational domain (not in scale).

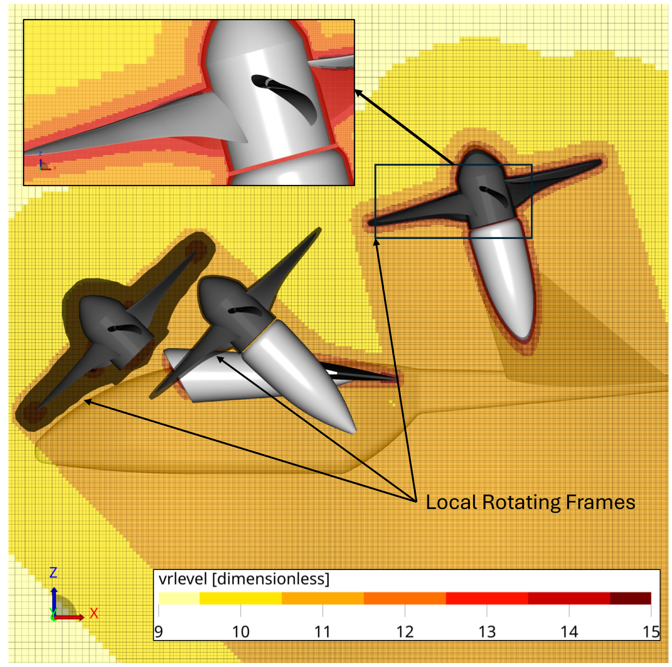


(b) Representation of finer VRs distribution.

Figure 1: Discretization of the simulation domain around the aircraft geometry.

mass center. These spheres are equally spaced by preserving the same number of voxels in the radial direction through levels.

Within the VR10 level, a dedicated surface was created enclosing the aircraft to implement the permeable formulation of the FW-H analogy. The surface was defined as an offset from the aircraft combined with 6 cylinders, one for each propeller, which have their axis normal to the rotor disc. In this way, the wake of propellers is included in the surface, avoiding spurious noise sources due to the direct interaction of the wake on the FW-H surfaces. In addition, two more permeable surfaces were defined in the same way, but with a small offset. Averaging the signals over these three surfaces allows further mitigation of spurious noise sources, especially those caused by the impact of the wake on the downstream region of the permeable surface (Refs. 27, 28). Lastly, a dedicated subregion within VR11, enclosing the propeller blades and spinner, was assigned a sliding-mesh local reference frame. This reference frame rotates at the prescribed propeller angular velocity relative to the stationary background domain.

# RESULTS

This section presents the results of the numerical simulations and is organized into three main parts. First, a grid convergence study is carried out to assess the sensitivity of the solution to mesh resolution and to ensure numerical accuracy. Subsequently, the aerodynamic performance of the vehicle is analyzed, with a focus on the flow-field characteristics. Finally, the acoustic signature is examined through far-field assessments, enabling evaluation of the noise emission associated with the simulated flight condition, namely the transition.

Table 1: Grid details of the mesh sensitivity study.

| Name | Voxels, M | SVS, mm | $\Delta t/T$, – |
|---|---|---|---|
| Coarse | 157.37 | 1.97 | $2.9406 \times 10^{-6}$ |
| Medium | 301.97 | 1.40 | $2.0879 \times 10^{-6}$ |
| Fine | 617.21 | 0.987 | $1.4755 \times 10^{-6}$ |
| Very Fine | 1313.24 | 0.699 | $1.0439 \times 10^{-6}$ |

## Mesh convergence study

The mesh structure adopted for all simulations corresponds to the configuration described in the previous section. To evaluate the sensitivity of the solution to spatial discretization, four different meshes were generated, each characterized by a refinement level defined through a geometric progression based on the smallest voxel size (SVS). Specifically, the spatial resolution was increased by employing a growth ratio of $\sqrt{2}$ between successive meshes.

It is important to note that the time step in the simulations is not defined manually. Instead, it is automatically determined by the local cell size, following the streaming requirements of the particle distribution function between adjacent cells, as dictated by the LBM. As a result, only the spatial resolution was varied in this study, while the temporal discretization was inherently adjusted by the solver. The key parameters defining each mesh configuration are summarized in Table 1.

The grid convergence study was carried out considering the thrust of each propeller normalized according to

$$C_T = \frac{T}{\rho_\infty n^2 D^4}. \quad (1)$$

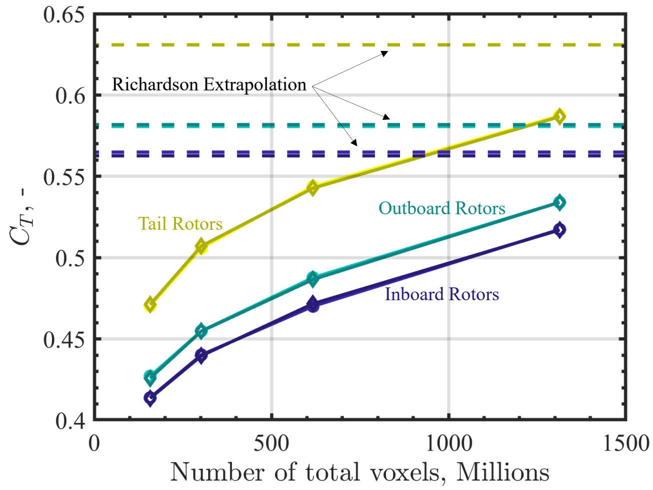


Figure 2: Grid convergence analysis with the exact solution estimated with Richardson extrapolation.

The results of the grid convergence study are presented in Figure 2. Richardson extrapolation (Refs. 29, 30) was performed to estimate the exact solution and to evaluate the convergence behavior of the mesh used in this study. The overall trend indicates that the simulations are approaching grid independence. However, full convergence, which would result in true grid independence, has not yet been achieved.

Despite this, the results obtained with the *very fine* mesh are considered acceptable, given their limited deviation from the Richardson-extrapolated solution. Consequently, the *very fine* mesh was used for all subsequent aerodynamic and acoustic analyses presented in the following sections.

The simulation using the *very fine* mesh required approximately 138 000 CPU hours, executed on five compute nodes, each equipped with 192 AMD EPYC™ 9654 processors. Although further mesh refinement would be of interest for increasing solution accuracy, the *very fine* mesh with its 1.3 billion voxels currently represents a practical upper limit due to computational cost constraints.

### Aerodynamic Loads and Flow Field

The grid convergence study revealed how the position in which the rotors are mounted affects their thrust. As would be expected because of the symmetry of the case, rotors symmetrically positioned with respect to the longitudinal axis of the aircraft produce the same thrust. In contrast, different rotor positions in the geometry of the aircraft have an impact on the ability of the rotors to generate thrust. In particular, the rotors mounted on the V-tail exhibit substantially higher thrust coefficients compared to those located on the main wing. This behavior is primarily attributed to the different tilt angles assigned to the V-tail rotors compared to the tilt angles of the main wing rotors. This, in fact, determines a higher advance ratio, which directly affects the blades loading and, consequentially, the produced thrust.

Upon examining the rotors installed on the main wing, a notable disparity in thrust is observed between the inboard and outboard units. This variation deserves further investigation, as it likely arises from the aerodynamic interaction with the wing structure located downstream of the rotor disks. At the same time, the wing itself is influenced by the rotor-induced wake, which alters the incoming flow and affects the local pressure distribution.

To better understand these mutual interactions, it is of particular interest to examine the pressure coefficient ($C_p$) distribution over the main wing and across the entire airframe. The $C_p$, whose distribution over the aircraft is represented in Figure 3, was averaged over the last revolution and is calculated according to

$$C_p = \frac{P - P_\infty}{\frac{1}{2}\rho_\infty V_\infty^2}. \quad (2)$$

An analysis of the pressure coefficient distribution on the upper surface of the main wing reveals several notable features. A wide region of low pressure is observed between the two inboard rotors, extending from the leading edge to approximately three-quarters of the chord length. This extended suction area is consistent with the upstream placement of the rotors, which are also tilted at 45°. In this configuration, the part of the wing located geometrically downstream of the retreating side of each rotor experiences an accelerated flow relative to the freestream, leading to increased suction on the wing surface.

Moving laterally between the inboard and outboard rotors, the $C_p$ distribution exhibits a more complex pattern: a region of increased pressure is followed by another localized suction area. This trend can be explained by the interaction of the rotor wakes in this region. Specifically, the pressure rise geometrically corresponds to the advancing side of the inboard rotor, where the induced flow decelerates, while the subsequent suction region aligns with the retreating side of the outboard rotor, where the flow accelerates.

Although this second interaction region is more localized compared to the broad suction area near the inboard rotors, it is nonetheless significant. The proximity to the retreating side of the inboard rotor implies that this region is also influenced by local flow deceleration, which further contributes to the complexity of the aerodynamic interaction.

To gain further insight into aerodynamic interactions and installation effects, a flow visualization based on the $\lambda_2$-criterion was performed to identify coherent vortical structures. The isosurfaces of $\lambda_2$, shown in Figure 4, reveal several key features related to rotor–airframe and rotor–rotor interactions. First, the wake generated by the V-tail rotors does not appear to impinge on the main wing, despite their 75° tilt angle. This behavior can be attributed to the flight condition considered in this study, which includes a forward flight velocity of 40 kts. The resulting free-stream effectively convects the V-tail rotor wakes away from the main lifting surfaces, thereby minimizing aerodynamic interference.

In contrast, significant aerodynamic interaction is observed in the forward section of the aircraft, particularly between the

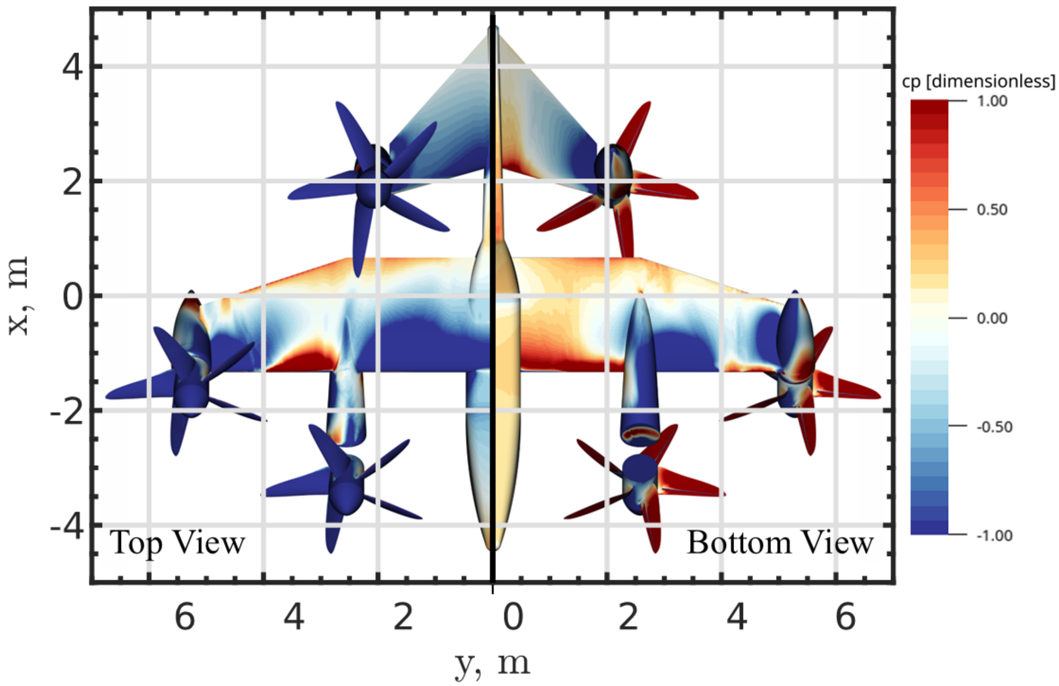


Figure 3: Surface pressure coefficient distribution over the aircraft. The colormap is selected to highlight suction regions on the wing surfaces. The left half of the image shows the aircraft from a top view, while the right half presents the bottom view.

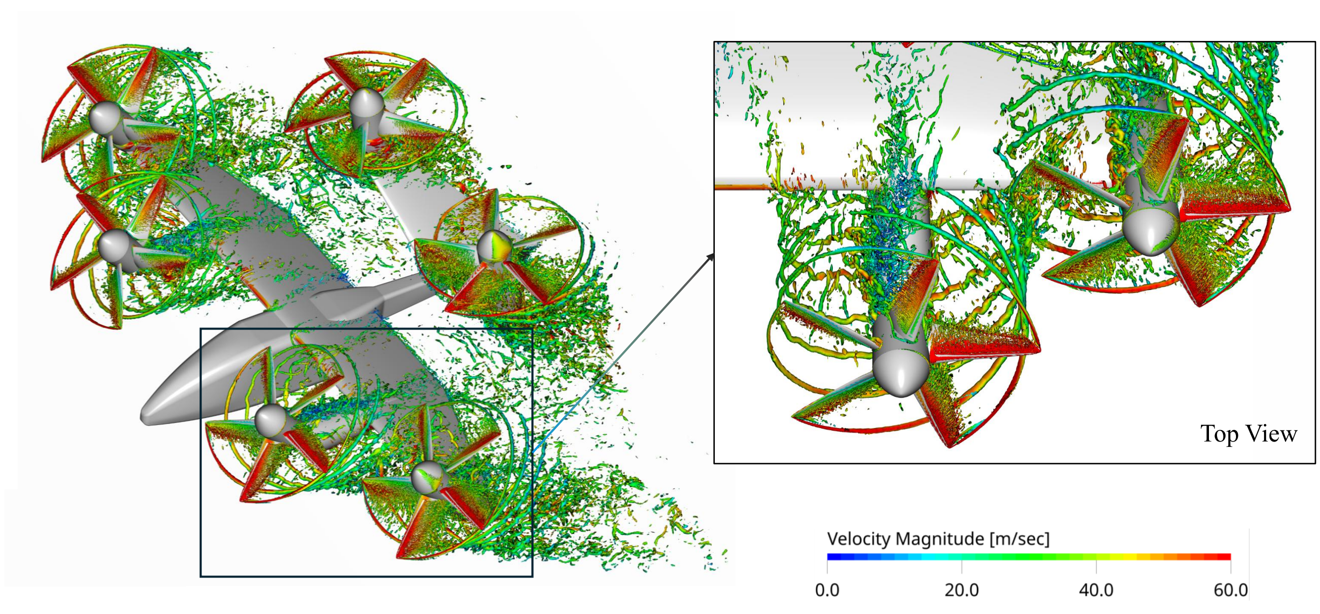


Figure 4: Vortex structures around the aircraft (isosurfaces of $\lambda_2$) with the colorbar highlighting the velocity magnitude. Detail of the rotor-rotor interaction.

front rotors, their supporting nacelles, and the wing. The $\lambda_2$ isosurfaces clearly show that the vortical structures generated by the rotor–nacelle system impinge directly on the wing surface. Furthermore, strong rotor–rotor interaction is evident between the inboard and outboard rotors on the same side of the vehicle. These interactions produce a highly disturbed flow region, which is subsequently advected onto the wing. The downstream impact of this distorted flow field on the wing surface produces the steep gradient in the pressure coefficient in the spanwise direction that was previously discussed.

Building on these observations, it is particularly insightful to analyze the aerodynamic loads acting on the main wing. The previous $C_p$ distribution and vortex interaction analysis already suggested the presence of non-uniform loading, especially in regions directly affected by rotor wakes and mutual rotor–rotor interactions. By examining the integrated aerodynamic forces along the wing span, it becomes possible to quantify the influence of these interactions and identify areas subjected to increased or asymmetric loading. To this end, the spanwise distribution of the aerodynamic lift and drag forces was calculated. These forces were non-dimensionalized by the dynamic pressure to facilitate interpretation and comparison across the wing. The resulting distributions are shown in Figure 5.

In both plots, the overall symmetry of the load distribution confirms that the aircraft setup and flow conditions produce symmetrical flow behavior on either side of the longitudinal axis. Focusing on the lift distribution, a strong positive loading is observed in the region between the inboard rotor and the fuselage. This corresponds to the extended low-pressure area on the upper surface of the wing previously identified in the $C_p$ analysis. Moving outward, a sharp inversion of the lift sign occurs at the location of the inboard rotor. The lift transitions from positive to negative, indicating a region of downforce. This behavior is attributed to the rotor tilt angle of 45°, which causes the advancing side of the rotor disk, positioned toward the wing tip, to deflect part of the flow downward onto the wing surface.

The resulting peak in negative lift is particularly pronounced, representing the highest magnitude of lift,in absolute terms, across the span. As we continue toward the tip, the lift increases again, showing a strong spanwise gradient and returning to positive values roughly midway between the inboard and outboard rotors. Near the outboard rotor, lift remains positive, but significantly lower in magnitude compared to the inboard region near the wing root.

Turning to the drag distribution, it is notable that the values are predominantly zero or negative along the entire span of the wing. This implies that, upon integration, the wing does not contribute to net drag; instead, it generates a forward-directed force, effectively acting as a source of thrust. The most pronounced negative peak is observed in correspondence with the advancing side of the inboard rotor. This region aligns with a significant area of low pressure on the lower surface of the wing, as previously identified in the underside view of the $C_p$ distribution.

However, it is important to emphasize that analyzing aerodynamic forces on the wing in isolation may be misleading. The wing and rotors should be considered as an integrated system. In earlier analyses, it was shown that the inboard rotors produce less thrust than their outboard counterparts, primarily due to aerodynamic interference with the wing. In this sense, the reduced thrust generated by the inboard rotors appears to be partially compensated by the wing's negative drag contribution, highlighting a redistribution of forces within the system rather than a net gain. In light of these findings, it becomes clear that the wing–rotor/propeller assembly must always be evaluated as a coupled subsystem to obtain a complete and accurate understanding of aerodynamic behavior and overall performance.

### Acoustics

The acoustic evaluation was carried out using the permeable formulation of the FWH equation in the frequency domain, as described earlier in the methodology section. To capture the radiated sound field, a spherical microphone array was defined, consisting of 1250 virtual receivers uniformly distributed over a sphere with a radius of 100 m. The array is composed of 25 parallels and 50 meridians, providing an angular resolution sufficient to capture directivity patterns.

The choice of a 100 m radius for the microphone sphere reflects a representative UAM scenario. In this configuration, the vehicle takes off from a vertiport located on the rooftop of a high-rise building and performs a vertical climb of approximately 30 m. The transition maneuver then occurs at an altitude of roughly 100 m above ground level. This setup allows for a realistic assessment of the noise propagated toward the ground, capturing the acoustic impact on the surrounding urban environment and its potential disturbance to the population.

The first acoustic metric evaluated is the overall sound power level (PWL) radiated by the aircraft during the simulated transition phase. The analysis was performed over a frequency range that spans from one-tenth to ten times the blade-passing frequency (BPF), with the BPF equal to 66.67 Hz. Based on the spherical microphone array described above and using the FWH formulation, the total PWL was found to be 127 dB.

Having such a single, global acoustic indicator is particularly valuable, as it enables a compact characterization of the vehicle's noise emissions. Moreover, it provides a useful reference for validating and calibrating lower-fidelity acoustic prediction tools, which may not capture the full complexity of high-fidelity simulations but can still benefit from reliable benchmark values.

To complement the overall PWL evaluation, the full sound power level spectrum was analyzed throughout the considered frequency range and is represented in Figure 6. The frequency spectrum of the PWL reveals that the dominant acoustic components are the tonal peaks associated with the blade passage frequency (BPF) harmonics. The first harmonic exhibits the highest magnitude, reaching 122 dB, and stands out

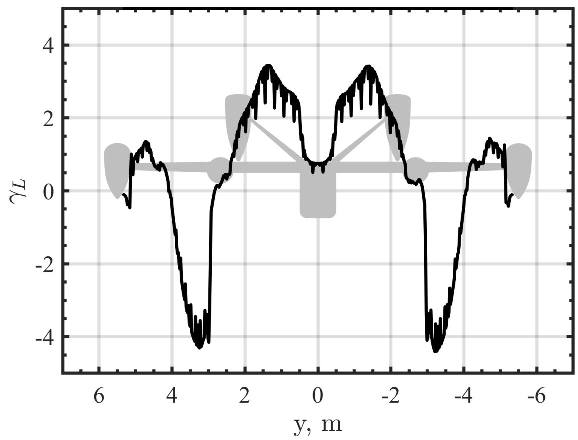


(a) Nondimensionalized lift.

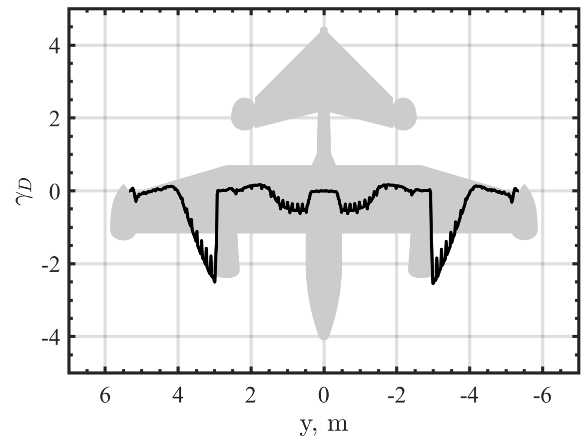


(b) Nondimensionalized drag.

Figure 5: Distribution of the aerodynamic forces across the wing span showing symmetry with respect to the longitudinal axis.

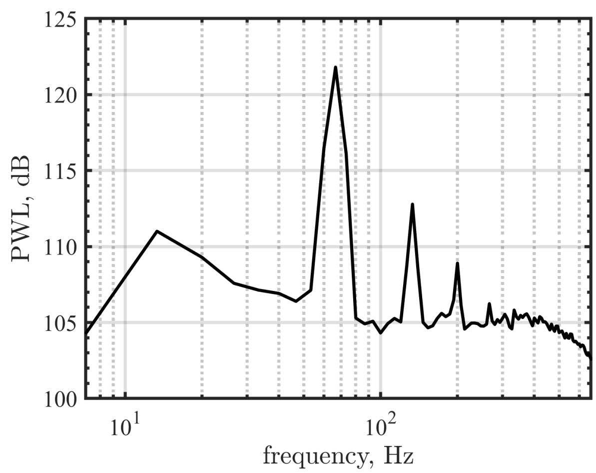


Figure 6: Sound power level spectrum computed over a 100 m radius sphere. The magnitude associated to the BPF (66.67 Hz) is 122 dB.

clearly from the rest of the spectrum. The second and third harmonics also show prominent peaks, with levels of 113 dB and 111 dB, respectively. Higher-order harmonics are still discernible, although progressively less pronounced: the fourth harmonic appears at 106 dB, while the fifth is barely visible and begins to merge with the surrounding broadband noise. The broadband component itself reaches substantial levels, exceeding 100 dB in the frequency bands considered in this analysis. However, a distinct decay trend is observable, starting well below 1 kHz. This is particularly relevant when considering A-weighted metrics, as frequencies above 1 kHz have a greater impact on human hearing. In this case, the fact that the PWL drops substantially before reaching this threshold suggests that the perceived loudness will be less severe, which is favorable from a perspective of human-compatibility.

To gain insight into the spatial distribution of the acoustic emissions, the radiation pattern of the sound pressure level (SPL) (Figure 7) was generated using data collected from the spherical microphone array surrounding the aircraft. This plot refers specifically to a narrow 7 Hz bandwidth centered on the blade-passing frequency, thereby highlighting the tonal radiation associated with the primary rotor harmonics.

The directional SPL distribution highlights two main regions of elevated acoustic emission: one located above and behind the aircraft, and another positioned in front and below. Given the focus on ground-level noise impact, a bottom-view projection (Figure 7b) was included to simulate the perspective of an observer on the ground. This view reveals that the highest SPL magnitude, reaching approximately 70 dB, are concentrated in a region directly ahead of the aircraft. Additionally, two symmetrical lobes of high magnitude are visible at approximately 30° relative to the flight direction.

To further investigate the spatial characteristics of the acoustic field, the overall sound pressure level (OASPL) was computed and visualized in the three main planes of the aircraft. The OASPL directivity plots were extracted from the spherical microphone array, which was previously described, and are represented in Figure 8.

In the frontal plane (x–z, Figure 8a), the noise levels are higher below the aircraft than above, although in both regions the OASPL remains close to 70 dB. Along the lateral directions (azimuthal angles of 0° and 180°), a reduction of approximately 6 dB is observed compared to the peak levels in the forward and aft directions.

In the longitudinal plane (*y*–*z*, Figure 8b), the highest OASPL values are concentrated between 90° and 150°, with a peak of 73 dB at 120°. Additionally, another region of elevated OASPL appears directly beneath the aircraft, around 270°, which warrants further investigation given its potential impact on ground observers. For this reason, the complete spectrum of the SPL measured by the microphone ($\theta = 270°$) directly below the aircraft, will be analyzed in the following.

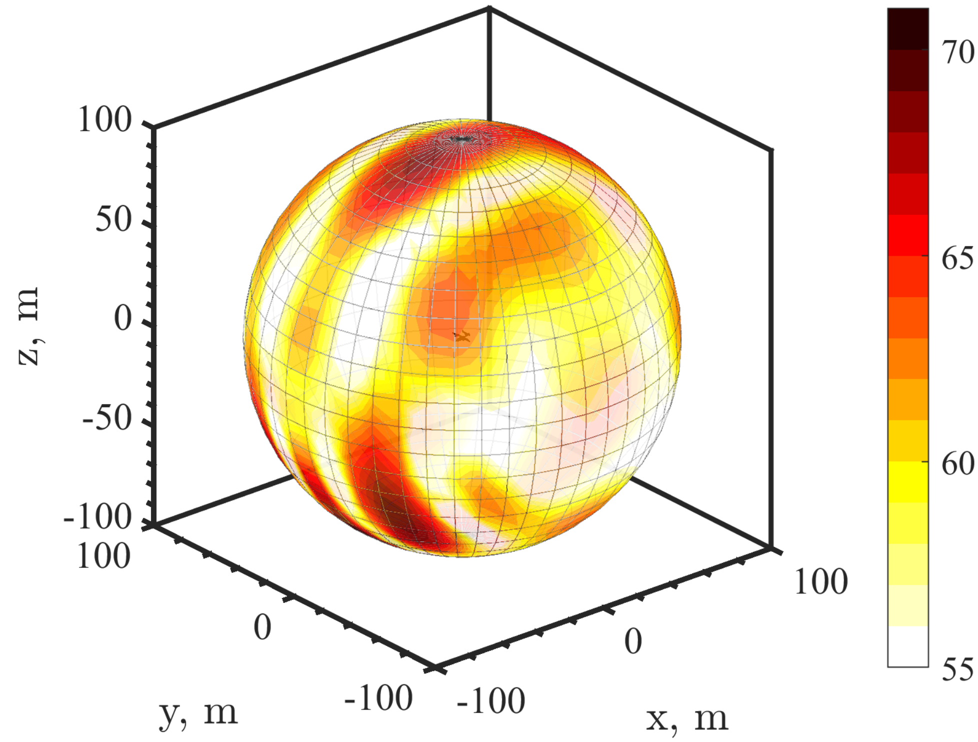


(a) Isometric view.

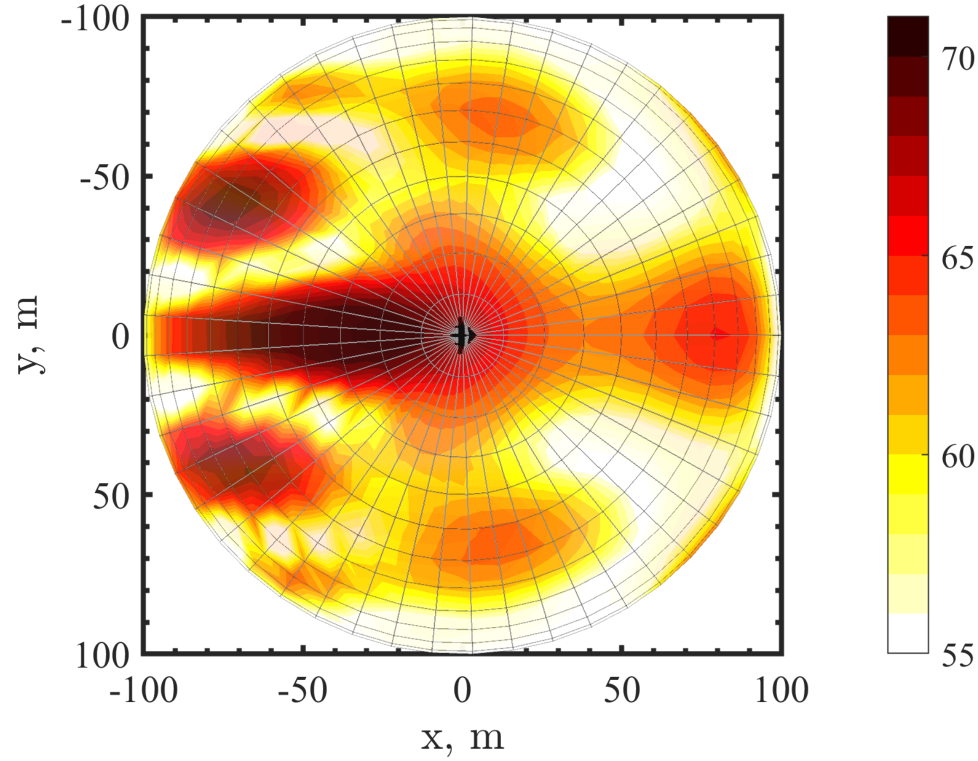


(b) Bottom view (aircraft flying above the observer).

Figure 7: Directional SPL plot over the 100 m spherical microphone array (aircraft not in scale).

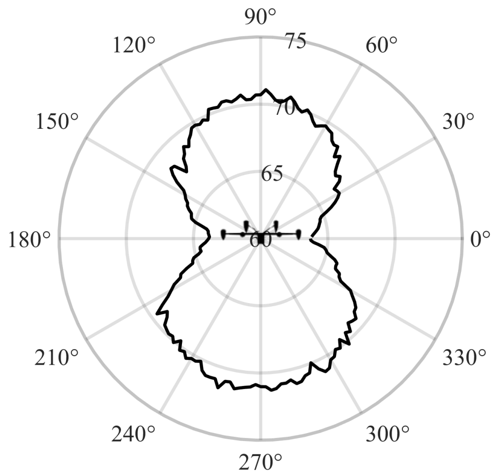


(a) *x*-plane.

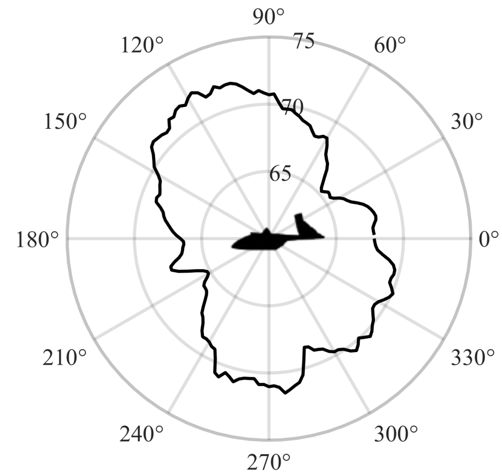


(b) *y*-plane.

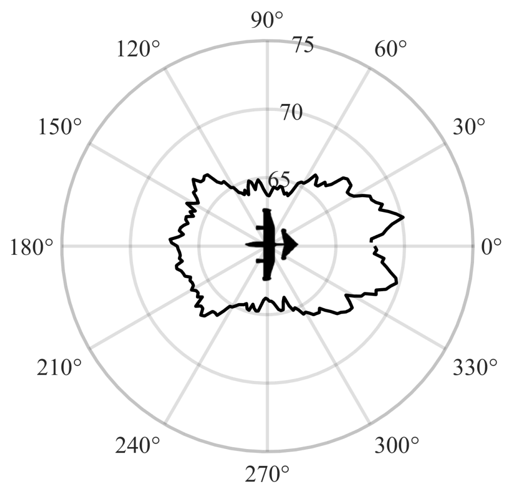


(c) *z*-plane.

Figure 8: OASPL directivity in the three main reference planes.

In contrast, the horizontal plane (*x*–*y*, Figure 8c) exhibits significantly lower OASPL. The values generally remain below 65 dB, except for two localized peaks observed downstream of the aircraft.

As mentioned previously, the microphone positioned directly beneath the aircraft in the longitudinal plane, at a distance of 100 m, is of particular interest and warrants further investigation. Located at ground level and having recorded a relatively high OASPL, it represents a critical point for assessing perceived noise by observers on the ground. For this reason, the full SPL spectrum at this location is analyzed in detail and presented in Figure 9.

The SPL spectrum measured at this ground-level location reveals that the dominant tonal component corresponds to the BPF, reaching a peak level of 66 dB. The second harmonic is significantly weaker, with a magnitude of 55 dB, which is only slightly above the broadband noise floor. No other harmonics are clearly distinguishable in the spectrum. The broadband noise remains relatively flat across the frequency range, with levels generally between 45 dB and 50 dB. Additionally, a secondary peak is observed at frequencies lower than the BPF. This feature is likely associated with other rotating components of the system, such as the rotor hub, and may warrant further investigation.

## CONCLUSIONS

The main conclusions of this study can be summarized as follows.

- A high-fidelity aeroacoustic simulation of a full-scale eVTOL vehicle performing the transition maneuver from vertical take-off to forward flight was successfully carried out using vLES and the Lattice Boltzmann Method.
- The chosen approach enabled the resolution of unsteady flow structures and their acoustic propagation, provid-

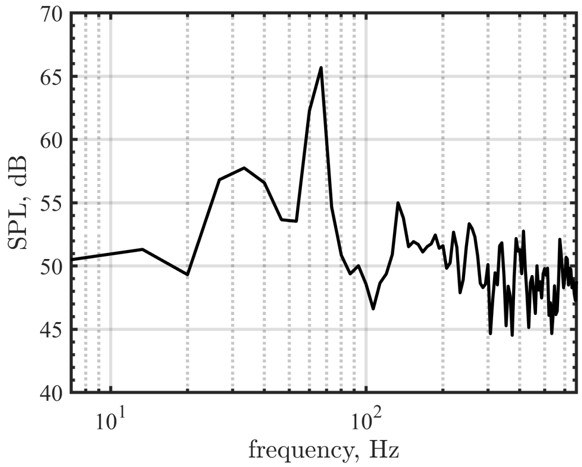


Figure 9: Sound Pressure Level spectrum measured at 100 m vertically below the aircraft ($\theta = 270°$ in the longitudinal plane).

ing a balanced trade-off between accuracy and computational cost.

- Aerodynamic interactions and installation effects were shown to strongly influence the force distribution across the aircraft, particularly highlighting the need to treat the rotor–nacelle–wing system as an integrated aerodynamic unit.
- The analysis of spanwise lift and drag distributions revealed complex flow–structure interactions, including thrust recovery mechanisms linked to rotor–wing interference.
- Far-field acoustic emissions were evaluated on a 100 m radius sphere using a permeable FW-H formulation, simulating a representative urban air mobility operational scenario.
- Noise radiation was characterized in terms of both overall and spectral sound power levels, with a computed total PWL of 127 dB over a frequency range of 0.1 to 10 times the blade-passing frequency.

The high-fidelity results generated in this work provide a valuable benchmark for the validation and improvement of low-fidelity noise prediction models commonly used in the early design phases.

Author contact: Federico Di Verniere, f.diverniere@tudelft.nl

## ACKNOWLEDGMENTS

This project has received funding from the European Research Council (ERC) under the European Union's Horizon research and innovation programme (MORASINA, grant agreement No. 101124038). Views and opinions expressed are however those of the author(s) only and do not necessarily reflect those of the European Union or the European Research Council Executive Agency. Neither the European Union nor the granting authority can be held responsible for them.

## REFERENCES


1. Society, V. F., "eVTOL Aircraft Directory," https://evtol.news/aircraft, [Accessed 10-07-2025].
2. Pascioni, K. A., Watts, M. E., Houston, M., Lind, A., Stephenson, J. H., and Bain, J., "Acoustic Flight Test of the Joby Aviation Advanced Air Mobility Prototype Vehicle," 28th AIAA/CEAS Aeroacoustics 2022 Conference, June 2022. DOI: 10.2514/6.2022-3036.
3. Zanotti, A., Velo, A., Pepe, C., Savino, A., Grassi, D., and Riccobene, L., "Aerodynamic interaction between tandem propellers in eVTOL transition flight configurations," *Aerospace Science and Technology*, Vol. 147, 2024, pp. 109017. DOI: https://doi.org/10.1016/j.ast.2024.109017.
4. Zhang, T., Barakos, G. N., Filippone, A., and Furqan, "High-fidelity aero-acoustic evaluations of a heavy-lift eVTOL in hover," *Journal of Sound and Vibration*, Vol. 584, August 2024, pp. 118453. DOI: 10.1016/j.jsv.2024.118453.
5. Bao, W., Wang, W., Chen, X., Zhang, H., and Zhao, Q., "Numerical analyses of aeroacoustic characteristics of tiltrotor considering the aerodynamic interaction by the fuselage in hover," *Aerospace Science and Technology*, Vol. 141, 2023, pp. 108558. DOI: https://doi.org/10.1016/j.ast.2023.108558.
6. Peters, J. L., Zevitas, C. D., Redline, S., Hastings, A., Sizov, N., Hart, J. E., Levy, J. I., Roof, C. J., and Wellenius, G. A., "Aviation Noise and Cardiovascular Health in the United States: a Review of the Evidence and Recommendations for Research Direction," *Current Epidemiology Reports*, Vol. 5, (2), April 2018, pp. 140–152. DOI: 10.1007/s40471-018-0151-2.
7. Hänninen, O., Knol, A. B., Jantunen, M., Lim, T.-A., Conrad, A., Rappolder, M., Carrer, P., Fanetti, A.-C., Kim, R., Buekers, J., Torfs, R., Iavarone, I., Classen, T., Hornberg, C., and Mekel, O. C., "Environmental Burden of Disease in Europe: Assessing Nine Risk Factors in Six Countries," *Environmental Health Perspectives*, Vol. 122, (5), May 2014, pp. 439–446. DOI: 10.1289/ehp.1206154.
8. European Union Aviation Safety Agency, "Drones & Air Mobility - Noise & Sustainability," https://www.easa.europa.eu/en/domains/drones-air-mobility/drones-air-mobility-landscape/noise-sustainability, [Accessed 10-07-2025].
9. Rizzi, S. A., Huff, D. L., Boyd, D. D., Bent, P., Henderson, B. S., Pascioni, K. A., Sargent, D. C., Josephson, D. L., Marsan, M., He, H. B., and Snider, R., "Urban Air Mobility Noise: Current Practice, Gaps, and Recommendations," https://ntrs.nasa.gov/citations/20205007433, October 2020.
10. Wang, S., Lima Pereira, L. T., and Ragni, D., "Design exploration of UAM vehicles," *Aerospace Science and Technology*, Vol. 160, May 2025, pp. 110058. DOI: 10.1016/j.ast.2025.110058.
11. Lima Pereira, L. T., Wang, S., and Ragni, D., "A Preliminary Design Framework for Performance and Noise Assessment

of Urban Air Mobility Vehicles," 30th AIAA/CEAS Aeroacoustics Conference (2024), May 2024. DOI: 10.2514/6.2024-3334.

12. Casalino, D., "Mitigation of Truncation Effects in Spectral Ffowcs-Williams and Hawkings Analogy," *AIAA paper 2024-3366*, 2024.

13. Teruna, C., Rego, L., Casalino, D., Ragni, D., and Avallone, F., "A Numerical Study on Aircraft Noise Mitigation Using Porous Stator Concepts," *Aerospace*, Vol. 9, 2 2022. DOI: 10.3390/AEROSPACE9020070.

14. Romani, G., and Casalino, D., "Rotorcraft blade-vortex interaction noise prediction using the Lattice-Boltzmann method," *Aerospace Science and Technology*, Vol. 88, 5 2019, pp. 147–157. DOI: 10.1016/J.AST.2019.03.029.

15. Avallone, F., Casalino, D., and Ragni, D., "Impingement of a propeller-slipstream on a leading edge with a flow-permeable insert: A computational aeroacoustic study," *International Journal of Aeroacoustics*, Vol. 17, 11 2018, pp. 687–711. DOI: 10.1177/1475472X18788961.

16. Romani, G., Ye, Q., Avallone, F., Ragni, D., and Casalino, D., "Numerical analysis of fan noise for the NOVA boundary-layer ingestion configuration," *Aerospace Science and Technology*, Vol. 96, 1 2020, pp. 105532. DOI: 10.1016/J.AST.2019.105532.

17. Lockard, D. P., Humphreys, W. M., Khorrami, M. R., Fares, E., Casalino, D., and Ravetta, P. A., "Comparison of Computational and Experimental Microphone Array Results for an 18%-Scale Aircraft Model," 21st AIAA/CEAS Aeroacoustics Conference, June 2015. DOI: 10.2514/6.2015-2990.

18. Fares, E., Casalino, D., and Khorrami, M. R., "Evaluation of airframe noise reduction concepts via simulations using a lattice boltzmann approach," *21st AIAA/CEAS Aeroacoustics Conference*, 2015. DOI: 10.2514/6.2015-2988.

19. Khorrami, M. R., Fares, E., and Casalino, D., "Towards full aircraft airframe noise prediction: Lattice boltzmann simulations," *20th AIAA/CEAS Aeroacoustics Conference*, 2014. DOI: 10.2514/6.2014-2481.

20. Casalino, D., van der Velden, W. C., Romani, G., and Gonzalez-Martino, I., "Aeroacoustic Analysis of Urban Air Operations Using the LB/VLES Method," 25th AIAA/CEAS Aeroacoustics Conference, May 2019. DOI: 10.2514/6.2019-2662.

21. Casalino, D., Romani, G., Pii, L. M., and Colombo, R., "Flow confinement effects on sUAS rotor noise," *Aerospace Science and Technology*, Vol. 143, December 2023, pp. 108756. DOI: 10.1016/j.ast.2023.108756.

22. Yunus, F., Casalino, D., Avallone, F., and Ragni, D., "Efficient prediction of urban air mobility noise in a vertiport environment," *Aerospace Science and Technology*, Vol. 139, August 2023, pp. 108410. DOI: 10.1016/j.ast.2023.108410.

23. Shao, W., and Li, J., "Review of lattice Boltzmann method applied to computational aeroacoustics," *Archives of Acoustics*, Vol. 44, 2019, pp. 215–238. DOI: 10.24425/AOA.2019.128486.

24. Lockard, D. P., "An efficient, two-dimensional implementation of the Ffowcs Williams and Hawkings equation," *Journal of Sound and Vibration*, Vol. 229, (4), 2000, pp. 897–911. DOI: https://doi.org/10.1006/jsvi.1999.2522.

25. van der Velden, W. C. P., Casalino, D., Gopalakrishnan, P., Jammalamadaka, A., Li, Y., Zhang, R., and Chen, H., "Validation of Jet Noise Simulations and Resulting Insights of Acoustic Near Field," *AIAA Journal*, Vol. 57, (12), December 2019, pp. 5156–5167. DOI: 10.2514/1.j057970.

26. Welch, P., "The use of fast Fourier transform for the estimation of power spectra: A method based on time averaging over short, modified periodograms," *IEEE Transactions on Audio and Electroacoustics*, Vol. 15, (2), 1967, pp. 70–73. DOI: 10.1109/TAU.1967.1161901.

27. Spalart, P. R., Belyaev, K. V., Shur, M. L., Strelets, M. K., and Travin, A. K., "On the differences in noise predictions based on solid and permeable surface Ffowcs Williams–Hawkings integral solutions," *International Journal of Aeroacoustics*, Vol. 18, (6-7), 2019, pp. 621–646. DOI: 10.1177/1475472X19878934.

28. Mendez, S., Shoeybi, M., Lele, S. K., and Moin, P., "On the Use of the Ffowcs Williams-Hawkings Equation to Predict Far-Field Jet Noise from Large-Eddy Simulations," *International Journal of Aeroacoustics*, Vol. 12, (1-2), 2013, pp. 1–20. DOI: 10.1260/1475-472X.12.1-2.1.

29. Richardson, L. F., and Gaunt, J. A., "The deferred approach to the limit," *Philosophical Transactions of the Royal Society of London Series A*, Vol. 226, (636-646), January 1927, pp. 299–361.

30. Roache, P. J., "Quantification of uncertainty in computational fluid dynamics," *Annual Review of Fluid Mechanics*, Vol. 29, (Volume 29, 1997), 1997, pp. 123–160. DOI: https://doi.org/10.1146/annurev.fluid.29.1.123.